

**Copyright**

**by**

**Jacob Preston Troutman**

**2019**

The Thesis Committee for Jacob Preston Troutman  
Certifies that this is the approved version of the following thesis:

The Synthesis of Randomly Alloyed Palladium–Silver  
Nanoparticles for the Catalytic Treatment of Aqueous  
Nitrite

APPROVED BY

SUPERVISING COMMITTEE:

Charles J. Werth, Supervisor

Simon M. Humphrey

**The Synthesis of Randomly Alloyed Palladium–Silver  
Nanoparticles for the Catalytic Treatment of Aqueous  
Nitrite**

by

**Jacob Preston Troutman**

**Thesis**

Presented to the Faculty of the Graduate School of

The University of Texas at Austin

in Partial Fulfillment

of the Requirements

for the Degree of

**Master of Science in Engineering**

The University of Texas at Austin

May 2019

## Acknowledgments

I would like to thank Dr. Pranaw Kunal (UT Austin, formerly) for all his teachings and patience while I learned how to synthesize nanoparticles. Additionally, I would like to thank Hongyu (Chris) Guo (UT Austin) for his assistance in characterizing nanoparticles. I would also like to thank Dr. Dwight Romanovicz (UT Austin; TEM), Dr. Karalee Jarvis (UT Austin; HR-TEM), and Dr. Vincent Lynch (UT Austin; PXRD) for analytical assistance.

# The Synthesis of Randomly Alloyed Palladium–Silver Nanoparticles for the Catalytic Treatment of Aqueous Nitrite

Jacob Preston Troutman, M.S.E.

The University of Texas at Austin, 2019

Supervisor: Charles J. Werth

Nitrate ( $\text{NO}_3^-$ ), and its daughter compound nitrite ( $\text{NO}_2^-$ ), are two of the most prevalent contaminants in drinking water. Catalytic degradation of  $\text{NO}_3^-$  and  $\text{NO}_2^-$  provides a treatment method with a small environmental footprint, though it is currently hindered by the need for a catalytic system that pairs reduced costs with enhanced activity and longevity. Monodisperse, randomly-alloyed palladium–silver nanoparticles ( $\text{Pd}_X\text{Ag}_{100-X}\text{NPs}$ ) with tunable compositions ( $X = 50\text{--}95$ ) were studied for use as catalysts in aqueous  $\text{NO}_2^-$  reduction. The synthesized  $\text{Pd}_X\text{Ag}_{100-X}\text{NPs}$  were supported on amorphous silica ( $\text{SiO}_2$ ) and studied for use as aqueous  $\text{NO}_2^-$  reduction catalysts in batch reactors with  $\text{H}_2$  gas as the electron donor. Nitrite reduction followed pseudo-first-order reaction kinetics for  $\geq 80\%$  conversion, and displayed a high selectivity ( $>98\%$ ) for nitrogen gas ( $\text{N}_2$ ) as the end product. Nearly all compositions displayed increased activity over pure PdNPs supported on amorphous  $\text{SiO}_2$ . Catalyst longevity was assessed for the most active catalyst. Throughout recycling, the catalytic activity decreased, although complementary analysis indicated no major physical changes of the catalyst. Overall, this work demonstrates that incorporating inexpensive, semi-noble metals into bimetallic alloys is a potential avenue for increasing catalytic activity while decreasing catalyst cost for  $\text{NO}_2^-$  reduction.

Keywords: *palladium–silver alloys, nitrite hydrogenation, heterogeneous catalysis, water treatment, microwave synthesis*

## Table of Contents

<b>List of Tables</b>	<b>ix</b>
<b>List of Figures</b>	<b>x</b>
<b>Chapter 1 Introduction</b>	<b>1</b>
1.1 Motivation . . . . .	1
1.2 Background . . . . .	4
<b>Chapter 2 Experimental Methods</b>	<b>9</b>
2.1 Materials . . . . .	9
2.2 Analytical Methods . . . . .	9
2.3 Synthesis of PdNP and PdAgNP Catalysts . . . . .	11
2.4 Kinetic Experiments and Modeling . . . . .	13
<b>Chapter 3 Results and Discussion</b>	<b>15</b>
3.1 Optimization of NP Synthesis . . . . .	15
3.2 Synthesis of Pd <sub>X</sub> Ag <sub>100-X</sub> NPs ( $X = 50-100$ ) . . . . .	19
3.3 Catalyst Performance and Recyclability . . . . .	23
<b>Chapter 4 Conclusions and Future Work</b>	<b>29</b>
<b>Appendices</b>	<b>31</b>
A Nanoparticle Optimization, Synthesis, and Characterization . . . . .	32
B Catalyst Performance . . . . .	35



## List of Tables

3.1	Average composition values of PdAgNPs . . . . .	20
3.2	Nitrite reduction selectivity of various SiO <sub>2</sub> -supported PdAgNPs . . .	25
B.1	Pseudo-first-order rate constants for NO <sub>2</sub> <sup>-</sup> reduction normalized to the total cost of metal used per catalyst. . . . .	35
B.2	Catalyst activities over repeated NO <sub>2</sub> <sup>-</sup> reduction cycles. . . . .	36

## List of Figures

1.1	Pd-catalyzed reduction mechanism of aqueous nitrate. . . . .	4
1.2	Catalytic reaction pathway of nitrate to nitrite. . . . .	5
3.1	TEM images comparing precursor injection rates. . . . .	16
3.2	TEM images examining the use of an external reducing agent. . . . .	17
3.3	TEM images examining the use of Pd(NO <sub>3</sub> ) <sub>2</sub> as the Pd precursor. . . . .	18
3.4	Representative TEM images showing Pd <sub>X</sub> Ag <sub>100-X</sub> NPs. . . . .	21
3.5	PXRD patterns for Pd <sub>X</sub> Ag <sub>100-X</sub> NPs. . . . .	22
3.6	HR-TEM and 2D-EDS images of synthesized Pd <sub>95</sub> Ag <sub>5</sub> NPs. . . . .	23
3.7	Total metal mass normalized first-order rate constants for PdAgNP-SiO <sub>2</sub> catalysts. . . . .	24
3.8	Catalytic activity comparison between Pd <sub>95</sub> Ag <sub>5</sub> NP-SiO <sub>2</sub> catalyst and pure PdNP-SiO <sub>2</sub> catalyst with multiple cycles of NO <sub>2</sub> <sup>-</sup> reduction. . . . .	27
A.1	Microwave set-up used for nanoparticle synthesis reactions. . . . .	32
A.2	Attempts to replicate PdAgNP synthesis with NaBH <sub>4</sub> and a <i>t</i> of 10 minutes. . . . .	32
A.3	Powder X-ray diffraction spectra of optimization PdAgNPs. . . . .	33
A.4	TEM image of Pd-poor nanoparticles. . . . .	33
A.5	PXRD patterns showing the shifting of the (111) Bragg reflection with respect to composition. . . . .	34

B.1	<i>Log</i> NO <sub>2</sub> <sup>-</sup> concentration vs. time curves for PdAgNP-SiO <sub>2</sub> catalyzed reduction reactions. . . . .	35
B.2	PXRD spectra comparing Pd <sub>95</sub> Ag <sub>5</sub> NPs before and after multiple NO <sub>2</sub> <sup>-</sup> reduction cycles. . . . .	36
B.3	TEM images of SiO <sub>2</sub> -supported Pd <sub>95</sub> Ag <sub>5</sub> NPs before and after multiple NO <sub>2</sub> <sup>-</sup> reduction cycles. . . . .	37

# Chapter 1: Introduction

## 1.1 Motivation

All of human life depends on having access to fresh water. In 2014, the United States alone consumed an estimated 345 billion gallons of fresh surface and groundwater per day for agriculture, energy production, human consumption, and other needs.<sup>(1)</sup> Anthropogenic activities, though, lead to millions of tons of chemical contaminants being released into the water supply every year.<sup>(2)</sup> Of these contaminants, nitrate ( $\text{NO}_3^-$ ) is one of the most prevalent.<sup>(3)</sup> Nitrate is a naturally occurring oxyanion present in many surface and groundwater sources in low levels.<sup>(4)</sup> However, these levels can often be heightened by man-made sources, such as livestock, septic systems, both industrial waste and wastewater discharge, and especially nitrogen-rich fertilizers.<sup>(3; 5; 6; 7)</sup> Because of its correlated adverse health effects,  $\text{NO}_3^-$  is regulated by both the United States Environmental Protection Agency (EPA) at a maximum contaminant level (MCL) of  $10 \text{ mg-N L}^{-1}$  and the World Health Organization (WHO) at a maximum level of  $11.3 \text{ mg-N L}^{-1}$ .<sup>(8)</sup> Once ingested,  $\text{NO}_3^-$  can be reduced *in vitro* to nitrite ( $\text{NO}_2^-$ ), which causes methemoglobinemia, or “blue-baby syndrome” in infants, the elderly, and the infirm. Nitrite can also react with amines and amides in the body to form *N*-nitroso compounds, which are known carcinogens.<sup>(4; 5; 7; 8)</sup>

Rural areas, especially those with shallow, domestic wells drawing from oxic groundwater, are especially at risk for  $\text{NO}_3^-$  contamination.<sup>(4; 9)</sup> These wells serve an estimated 45 million people in the United States.<sup>(10; 11)</sup> A study of 2388 domes-

tic wells by the National Water-Quality Assessment Program of the U.S. Geological Survey (USGS) found that  $\text{NO}_3^-$  levels exceeded the MCL in 7% of the wells.<sup>(9)</sup> A previous similar study of 1255 wells reported  $\text{NO}_3^-$  levels above the MCL in 11% of domestic wells.<sup>(10)</sup> Nitrate is so prevalent that it is detectable in nearly 70% of groundwater samples, more than 13 times as common as other contaminants, such as nitrite, ammonia, organic nitrogen, or orthophosphate.<sup>(12)</sup> Regional and state-wide studies throughout the United States present similar results, despite the varied geographies and climates. A common linkage in all of the studies was privately-owned, unregulated, shallow wells.<sup>(3; 8; 13)</sup> However,  $\text{NO}_3^-$  contamination is not limited to just the United States, and countries around the world, both developed and developing, are facing  $\text{NO}_3^-$ -contaminated water crises.<sup>(4; 8; 14; 15; 16)</sup>

Currently, the predominant method for the removal of  $\text{NO}_3^-$  from drinking water is ion exchange (IX). Ion exchange works by passing contaminated water over a strong base anion (SBA) resin bed, typically loaded with either chloride ( $\text{Cl}^-$ ) or bicarbonate ( $\text{HCO}_3^-$ ), that exchanges the loaded anion for  $\text{NO}_3^-$ .<sup>(14)</sup> Ion exchange efficiently removes  $\text{NO}_3^-$  from drinking water. Once the resin's exchange capacity is reached, though, the resin must be regenerated, which requires a highly concentrated brine solution. Regeneration results in a secondary waste stream that must be disposed or properly treated.<sup>(14; 17)</sup> The salt requirement for the regeneration is one of the biggest costs for IX. Over a 20-year lifespan of an IX plant, salt costs alone can be double the initial equipment costs.<sup>(14)</sup> In fact, salt can account for an estimated 77% of the total operational and maintenance costs for IX systems.<sup>(18)</sup> A drinking water plant treating 2.5 MGD requires about 8.2 metric tons of salt per day

for maintenance. Disposal of the regeneration waste brine also raises environmental concerns. Discharge of such highly concentrated solutions into surface waters or sewers is also highly regulated by local ordinances, which limits the viability of IX systems.<sup>(19)</sup> Ion exchange also has drawbacks when treating water with high levels of organic matter or other anion contaminants, such as sulfate ( $\text{SO}_4^{2-}$ ). The common order for increasing ion selectivity of resins is  $\text{HCO}_3^-$ ,  $\text{Cl}^-$ ,  $\text{NO}_3^-$ , and then  $\text{SO}_4^{2-}$ . Because of this, the presence of  $\text{SO}_4^{2-}$  limits the capacity of typical resins for  $\text{NO}_3^-$ .<sup>(14)</sup> Despite the effectiveness of ion exchange systems for  $\text{NO}_3^-$  removal, they face major limitations due to their significant environmental footprints, high operational costs, and issues with highly contaminated water.

Other emerging technologies for  $\text{NO}_3^-$  removal in drinking water include biological denitrification, chemical denitrification, reverse osmosis (RO), electrodialysis (ED), and catalytic treatment. Both RO and ED show promise in small-scale systems. However, both processes are extremely power intensive which limits the current scalability. Chemical denitrification shows limited promise, as it often results in large amounts of solid chemical waste (e.g., iron sludge) and has high material costs.<sup>(14)</sup> Biological denitrification involves the use of microorganisms to reduce  $\text{NO}_3^-$  to di-nitrogen gas ( $\text{N}_2$ ). The major hindrance to biological denitrification is the long start-up time often required for these systems to achieve sufficient biomass growth. This growth can take weeks, or even months, which is problematic if  $\text{NO}_3^-$  treatment is only intermittently needed.<sup>(20; 21)</sup> Additionally, biological treatment raises concerns over increased chlorine usage, the possibility of introducing pathogens to public water supplies, and the formation of  $\text{NO}_2^-$  intermediates.<sup>(14; 17)</sup> Catalytic treatment directly

eliminates  $\text{NO}_3^-$  by reduction to  $\text{N}_2$  or ammonium ( $\text{NH}_4^+$ ) using atomic hydrogen, and so there is no generation of a secondary waste as with IX. Additionally, start-up times are a fraction of those required for biological treatment, and using hydrogen gas ( $\text{H}_2$ ) has been shown to have a substantially lower environmental footprint than the organic electron donors used in biological denitrification. Catalysis is also advantageous in that it requires much less energy than processes like RO or ED.<sup>(2; 17; 22)</sup> Currently though, application of an economically feasible and environmentally sustainable  $\text{NO}_3^-$  catalytic treatment technology is hindered by the need for a catalyst system with acceptable activity and longevity.<sup>(17; 19; 23)</sup>

## 1.2 Background

The proposed reaction scheme by which  $\text{NO}_3^-$  is catalytically reduced is shown in [Figure 1.1](#).<sup>(22)</sup> The first step is the reduction of adsorbed  $\text{NO}_3^-$  to adsorbed  $\text{NO}_2^-$ ,

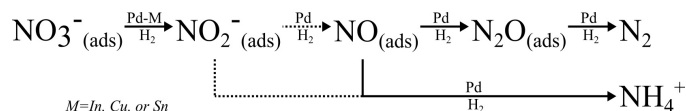


**Figure 1.1:** Accepted pathways for Pd-catalyzed nitrate reduction in aqueous solutions.

which requires two metals, while the subsequent steps do not. The first metal is a platinum-group metal (PGM) capable of facile activation of  $\text{H}_2$ . The second metal is a promoter metal (M) that individually is unable to activate  $\text{H}_2$ .<sup>(24)</sup> The promoter metal facilitates the reduction of  $\text{NO}_3^-_{(\text{ads})}$  via metal oxidation, before being re-reduced by activated “spillover” hydrogen from the PGM, as shown in [Figure 1.2](#).<sup>(25)</sup> The  $\text{NO}_2^-_{(\text{ads})}$  then migrates to a PGM site where it is further reduced to

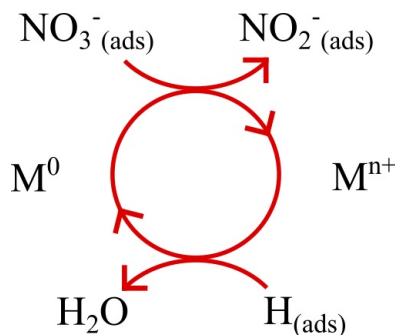


**Figure 1.2:** Nitrate catalytic reaction pathway to nitrite on PGM surface with M (Cu, In, Sn) as a secondary promoter metal and activated hydrogen as a reducing agent.

either  $\text{N}_2$  or  $\text{NH}_4^+$ , of which  $\text{N}_2$  is preferred in drinking water treatment.<sup>(2; 25; 26; 27)</sup> The production of  $\text{N}_2$  versus  $\text{NH}_4^+$  is determined by the ratio of adsorbed  $N$ -species to adsorbed  $H$ -species.<sup>(28; 29)</sup> This ratio of  $N:H$  is strongly affected by reaction conditions that influence the surface charge of the catalyst metal, the anions present that compete for adsorption, and the concentration of dissolved  $\text{H}_2$ . For example, increasing system pH leads to decreased surface charge and higher concentrations of hydroxide ( $\text{OH}^-$ ) ions. This in turn decreases the adsorption of both  $\text{NO}_3^-$  and  $\text{NO}_2^-$ , limiting reduction rates.<sup>(17; 28; 30)</sup> This lack of adsorbed  $N$ -species also decreases  $N:H$  surface coverage, increasing  $\text{NH}_4^+$  production as the adsorbed  $N$ -species are more likely to form  $N-H$  bonds than  $N-N$  bonds.<sup>(27)</sup> Furthermore, species like  $\text{HCO}_3^-$  that have similar geometries can compete with  $\text{NO}_3^-$  and  $\text{NO}_2^-$  for adsorption sites and increase  $\text{NH}_4^+$  production.<sup>(31)</sup> Higher concentrations of dissolved  $\text{H}_2$  also lead to increased  $\text{NH}_4^+$  selectivity for both  $\text{NO}_3^-$  and  $\text{NO}_2^-$  reduction. As the amount of dissolved  $\text{H}_2$  present increases, the surface concentration of activated adsorbed hydrogen ( $\text{H}^*$ ) also increases and the  $N:H$  surface coverage decreases. Thus, reaction

conditions that lead to higher dissolved  $\text{H}_2$  concentrations (e.g., high  $\text{H}_2$  gas flow rates) lead to an increase in  $\text{NH}_4^+$  production.<sup>(27; 32)</sup>

Beginning in 1993, Hörold and co-workers announced the first development of a selective catalyst system for  $\text{NO}_3^-$  and  $\text{NO}_2^-$  removal in drinking water, demonstrating the ability of multiple platinum-group metals to catalytically reduce  $\text{NO}_2^-$ . They observed the highest activity in platinum (Pt), but with a mixture of end products. Ruthenium (Ru), iridium (Ir), and rhodium (Rh) displayed low activities and were highly selective towards  $\text{NH}_4^+$ . Palladium (Pd), though, demonstrated moderate activity with a promising  $\text{N}_2$  selectivity. They then paired Pd with various promoter metals to investigate  $\text{NO}_3^-$  reduction. Of these, copper (Cu) yielded both the highest  $\text{NO}_3^-$  reduction activity and  $\text{N}_2$  selectivity.<sup>(32)</sup> However, recent work has shown that using indium (In) as the promoter metal can afford similar  $\text{NO}_3^-$  reduction rates and selectivities. Additionally, Pd-In catalysts have proven more stable against metal leaching compared to Pd-Cu catalysts.<sup>(33; 34)</sup> In the intervening decades, much has been done to tailor catalyst design on the molecular level in an attempt to optimize Pd-based aqueous  $\text{NO}_3^-$  reduction, including regulating Pd and promoter metal surface coverage on supports,<sup>(35; 36)</sup> using various carbon supports<sup>(37; 38)</sup> and metal oxide supports<sup>(39; 40; 41)</sup> that provide unique electronic interactions such as electron delocalization or strong metal-support interactions (SMSI), controlling nanoparticle shape and exposed facets,<sup>(42)</sup> and combining palladium with catalytically inactive metals (gold, Au, or Cu) at the atomic level.<sup>(29; 43)</sup>

Recently, studies have shown that randomly alloying catalytically active PGMs (such as Pd and Rh) with catalytically inactive group 11 metals (Cu, Ag, Au) can

provide enhanced activity over pure PGMs or non-alloyed bimetallic systems. These solid-solution alloys take advantage of d-band electron mixing and ensemble effects to alter adsorbate binding strengths to the metal alloy surface.<sup>(44; 45)</sup> These alloyed catalysts have mostly been studied for gas-phase reactions. Chen and co-workers demonstrated the benefits of PdAu alloys for the acetoxylation of ethylene.<sup>(46)</sup> PdAu, RhAu, and RhAg alloys have been studied as gas-phase hydrogenation catalysts, as well.<sup>(47; 48)</sup> Despite gold and silver both being inactive for hydrogenation catalysis, these alloys have displayed increased activity over pure Pd or Rh catalysts. Density functional theory (DFT) calculations show that ensemble effects between the active and inactive metal sites create more favorable binding conditions for hydrogen and alkene species, thus promoting more rapid reactions. More recently, alloyed PdAu nanoparticles (PdAuNPs) have been shown to exhibit increased activity for aqueous-phase hydrogenation of  $\text{NO}_2^-$  as compared to pure Pd-based catalysts.<sup>(17)</sup> Similar to gas-phase hydrogenation, these PdAuNPs take advantage of sub-atomic interactions between the palladium and gold atoms to promote  $\text{NO}_2^-$  reduction. However, at \$41 per gram (APMEX, Inc; May 2019), gold is nearly as expensive as palladium (\$44 per gram; APMEX, Inc; May 2019), and so these catalysts do little to address the financial concerns associated with catalyst systems for water treatment.

Silver provides an attractive alternative for gold in alloyed bimetallic catalysts. Like gold, silver is a group 11,  $d^9$  metal. The price of silver, \$0.48 per gram (APMEX, Inc; May 2019), is a fraction of the price of gold. The goal of the following work is to investigate palladium–silver nanoparticles (PdAgNPs) as potential catalysts for aqueous-phase  $\text{NO}_2^-$  hydrogenation. To achieve this goal, the synthesis

of PdAgNPs using a microwave-assisted polyol reduction method will be optimized to create a series of NPs with Pd:Ag ratios from 1:1 to 9:1. The PdAgNPs will then be loaded onto amorphous silica ( $\text{SiO}_2$ ) and evaluated for  $\text{NO}_2^-$  reduction in batch reactors. Amorphous  $\text{SiO}_2$  allows for easier handling and recovery of the NP catalysts; however, it is relatively chemically inert and thus should not influence the catalytic properties of the synthesized NPs.<sup>(47; 49; 50)</sup> To address the longevity of the catalyst system, the most active catalyst composition will be subjected to multiple reduction cycles. The synthesized catalysts will be characterized using powder X-ray diffraction (PXRD), high- and low-resolution transmission electron microscopy (TEM), inductively coupled plasma optical emission spectroscopy (ICP-OES), and energy dispersive X-ray spectroscopy (EDS) to determine how nanoparticle composition effects  $\text{NO}_2^-$  hydrogenation activity.

## Chapter 2: Experimental Methods

### 2.1 Materials

All materials were used as received with no further purification or treatment.  $\text{K}_2\text{PdCl}_4$  (99%; Acros Organics),  $\text{Pd}(\text{NO}_3)_2 \cdot n\text{H}_2\text{O}$  (99.9%; Strem Chemicals),  $\text{AgNO}_3$  (99.9%; Alfa Aesar), *poly*(vinylpyrrolidone) (PVP;  $\{\text{C}_6\text{H}_9\text{NO}\}_n$ ;  $\langle M_w \rangle = 58000$ ; Alfa Aesar),  $\text{NaBH}_4$  (98%; Alfa Aesar), and ethylene glycol (EG; 99.8%; Fisher Scientific) were used for all nanoparticle synthesis reactions. Pluronic<sup>®</sup> P-123, *poly*(ethylene glycol) ( $\langle M_w \rangle = 5800$ ; Sigma-Aldrich), HCl (12.1 M; Fisher Scientific), *n*-decane (99%; Acros Organics),  $\text{NH}_4\text{F}$  (96%; Alfa Aesar), and tetraethyl orthosilicate (TEOS;  $\text{Si}(\text{OC}_2\text{H}_5)_4$ ; 98%; Alfa Aesar) were used to synthesize the amorphous  $\text{SiO}_2$  support.  $\text{NaNO}_2$  (99%; Sigma-Aldrich) was used as the nitrite source for kinetic experiments.  $\text{KH}_2\text{PO}_4$  (99%; Sigma-Aldrich) and  $\text{K}_2\text{HPO}_4$  (98%; Sigma-Aldrich) were used as pH control for kinetic reactions.  $\text{H}_2$  gas (99.99%+; Praxair) was used as the electron donor for kinetic experiments. All reagents and solvents were analytical grade unless otherwise stated.

### 2.2 Analytical Methods

Powder X-ray diffraction (PXRD) measurements were performed using a R-Axis Spider diffractometer (Rigaku Corporation) equipped with a  $\text{CuK}\alpha$  source ( $\lambda = 1.5418 \text{ \AA}$ ) operated at 40 kV and 40 mA. Transmission electron microscopy (TEM) samples were prepared by dispersing NPs in ethanol and drop-casting the disper-

sion onto 200 mesh copper Formvar grids (Ted Pella, Inc.) before air-drying the sample. Nanoparticle size was analyzed by manually measuring particles using the imaging software Image-J (<https://imagej.nih.gov/ij/>); for each sample, a minimum of 300 measurements were taken in order to calculate a mean particle diameter and corresponding standard deviation. Low-resolution TEM (LR-TEM) images were obtained using a FEI Tecnai transmission electron microscope operated at 80 kV. High-resolution TEM (HR-TEM) images and energy dispersive X-ray spectroscopy (EDS) spectra were obtained using a JEOL 2010F transmission electron microscope equipped with an Oxford EDS detector and operated at 200 KeV with a 0.19 nm point to point resolution.

Percent metal loading and bulk elemental analysis of catalysts were determined by inductively coupled plasma optical emission spectroscopy (ICP-OES) on a Varian 710-ES (Agilent Technologies, Inc.) using the ICP Expert II Software (Agilent). Samples were prepared for ICP-OES by digesting 5 mg of each catalyst in nitric acid ( $\text{HNO}_3$ ; 6  $\text{cm}^3$ ; trace metal grade) heated to 100 °C. Samples were diluted to 25  $\text{cm}^3$  and left over night to allow support material to settle before 11  $\text{cm}^3$  of the solution were collected.  $\text{NO}_2^-$  concentrations were determined by ion chromatography (IC) using a Dionex ICS-2100 equipped with a Dionex IonPac AS18 column and a Dionex EGC II KOH EluGen Cartridge (run under program-controlled concentration with a flow of 1  $\text{cm}^3 \text{ min}^{-1}$ ).  $\text{NH}_3$  concentrations were measured via Hach colorimetric kits using the salicylate method (0.02–2.50  $\text{mg L}^{-1} \text{ NH}_3\text{-N}$ ). The measurement of pH was performed with a FiveEasy Plus Benchtop pH-Conductivity Meter (Mettler Toledo).

### 2.3 Synthesis of PdNP and PdAgNP Catalysts

$\text{Pd}_X\text{Ag}_{100-X}$ NPs, with the variable “ $X$ ” representing the molar percent of Pd present in the alloy, were synthesized using the following method adapted from previous work.<sup>(17; 47)</sup> The nanoparticles were synthesized by the polyol reduction method using microwave-assisted heating,  $\mu\text{wI}$ , as described in previous publications.<sup>(48; 51; 52; 53)</sup> All  $\mu\text{wI}$  reactions were carried out in a MARS 5 microwave reactor with a maximum power of 1600 W (2.45 GHz) (CEM Corp.). The reactions were carried out with fiber-optic temperature feedback control (RTP300+ temperature sensor; CEM Corp.) and magnetic stirring (450 rpm), while open to air. Generally, excess PVP (5–20 equiv of monomers per mmol of Pd + Ag) and  $\text{NaBH}_4$  (0–1 equiv per mmol of Pd + Ag) were dissolved in EG (15  $\text{cm}^3$ ), and the solution heated over 6 min to 150 °C with  $\mu\text{wI}$  under stirring. Separately, metal precursor salt(s) (0.10 mmol total metal, Pd + Ag) were dissolved in pre-solvent (5  $\text{cm}^3$ ) with sonication. The metal solution was then added directly to the hot PVP- $\text{NaBH}_4$ /EG solution via disposable PTFE tubing (i.d. 1.0 mm) by a programmable syringe pump (WPI, Inc) at a rate of 300  $\text{cm}^3 \text{h}^{-1}$ . After complete addition (30 s), the reaction was held under constant temperature and stirred for time  $t$ . At the end of reaction ( $t + 6.5$  min), the reaction flask was quickly transferred to an ice-water bath to quench the reaction. The resulting NPs were then isolated with the addition of acetone (ca. 70  $\text{cm}^3$ ) and centrifugation (5500 rpm; 5 min). The supernatant was then discarded, and the NPs re-dispersed in ethanol (10  $\text{cm}^3$ ) with sonication to remove excess PVP. The NPs were again isolated by precipitating with hexanes (ca. 80  $\text{cm}^3$ ) and centrifugation. The supernatant was poured off, and the nanoparticles were left to air dry overnight before being stored

in 50 mL polypropylene tubes as a glassy film.

Amorphous SiO<sub>2</sub> was prepared based on published methods.<sup>(54; 55)</sup> Pluronic<sup>®</sup> P-123 (2.4 g) was dissolved into an HCl solution (86 g; 1.03 M) and stirred (450 rpm) at 40 °C until all polymer was dissolved (the solution was clear). *n*-Decane (30 cm<sup>3</sup>; 0.154 mol) was added as the swelling agent, and the solution was stirred (1000 rpm) to homogeneity (at least 2 hours). NH<sub>4</sub>F (0.028 g; 0.76 mmol) was added, immediately followed by drop-wise addition of TEOS (5.6 cm<sup>3</sup>; 25.1 mmol). Stirring at 40 °C was continued for 20 h resulting in an opaque slurry. This slurry was transferred into a polyethylene bottle and placed into a static convection oven at 100 °C for 48 h, before being filtered. The isolated solid was repeatedly washed with distilled water to remove excess surfactant and then calcined at 550 °C for 6 h in a box furnace.

Catalysts were prepared by direct deposition of synthesized nanoparticles onto the synthesized silica to achieve approximately 1.5 wt% total metal loading. Briefly, amorphous silica (250 mg) was suspended in distilled water (10 cm<sup>3</sup>) by sonication and rapid stirring (1200 rpm) in a 20 cm<sup>3</sup> glass scintillation vial with a micro magnetic stir bar. Separately, 5.3 mg PVP-capped Pd<sub>*X*</sub>Ag<sub>100-*X*</sub>NPs or PdNPs were dispersed in ethanol (10 cm<sup>3</sup>) via sonication. NP suspensions were then added drop-wise to the SiO<sub>2</sub>/H<sub>2</sub>O suspension. The resulting mixtures were then stirred for 10 min (800 rpm) and sonicated for 10 min. This process was repeated for at least three more cycles, until the supernatant was clear. The supported NP catalysts were then isolated using vacuum filtration in air, extensively washed with water and ethanol, and then dried in a 60 °C oven overnight.

## 2.4 Kinetic Experiments and Modeling

$\text{NO}_2^-$  reduction experiments were carried out in batch-scale reactors. The reactions were performed at ambient temperature ( $23 \pm 1$  °C) and atmospheric pressure with magnetic stirring in 60 cm<sup>3</sup> glass vials sealed with a rubber septum. Phosphate buffer (40 cm<sup>3</sup>; pH 6.4) and supported NP catalyst (0.5 g L<sup>-1</sup>) were added to the reaction vessel. The suspension was sparged by bubbling with H<sub>2</sub> gas (0.120 L min<sup>-1</sup>) for a minimum of 1 h to ensure both medium and headspace were saturated. The reaction was initiated by spiking with a 100 μL aliquot of NaNO<sub>2</sub> (0.87 M) to give an initial concentration of 100 mg L<sup>-1</sup> NO<sub>2</sub><sup>-</sup> in the reaction flask. Samples were taken at regular time intervals for a total reaction time of 2 h for N-species analysis. The total volume of sample removed was ≤10% of the total solution volume, and it was assumed the catalyst concentration in the reactor remained constant throughout the reaction as the suspension was homogeneously dispersed. NO<sub>2</sub><sup>-</sup> reduction experiments were conducted in triplicate to derive rate constants for each unique catalyst composition. To test catalyst longevity, a series of five consecutive NO<sub>2</sub><sup>-</sup> reduction reactions were performed. At the end of each reaction, the catalyst suspension was re-sparged with H<sub>2</sub> gas for 1 h, before being re-spiked with a new aliquot of NO<sub>2</sub><sup>-</sup> (100 mg L<sup>-1</sup>). Again, the catalyst concentration was assumed constant as the samples were removed from a well-mixed flask with a homogeneous mixture.

NO<sub>2</sub><sup>-</sup> reduction was found to obey pseudo-first-order kinetics for consumption of greater than 80% of the initial NO<sub>2</sub><sup>-</sup> concentration. Initial first-order rate constants were normalized to the percent total metal concentration (Pd + Ag) for each catalyst

tested. The rate constants were obtained from the linear regression of the natural log of  $\text{NO}_2^-$  concentration versus time plots, using the equation

$$-\frac{dC_{\text{NO}_2^-}}{dt} \left( \frac{1}{C_M} \right) = k_{obs} C_{\text{NO}_2^-}$$

where  $C_{\text{NO}_2^-}$  is the concentration of aqueous nitrite ( $\text{mg NO}_2^- \text{ L}^{-1}$ ),  $C_M$  is the concentration of metal catalyst ( $\text{g}_{\text{metal}} \text{ L}^{-1}$ ), and  $k_{obs}$  is the observed first-order rate constant normalized by the metal catalyst concentration ( $\text{L g}_{\text{metal}}^{-1} \text{ min}^{-1}$ ).

## Chapter 3: Results and Discussion

### 3.1 Optimization of NP Synthesis

To start, the synthesis of randomly alloyed PdAgNPs with  $\mu$ w-assisted heating was optimized by examining the effects of precursor injection rate, an external reducing agent, metal precursor choice, and capping agent concentration. Optimization of a reproducible synthesis system was done with a 1:1 target composition of Pd:Ag. A major challenge of the PdAg system is the co-formation of silver salt precipitates during nanoparticle synthesis. These by-products provide major hindrances to monodisperse nanoparticle growth because they present various nucleation sites with different chemical environments, as well as result in colloidal AgCl or Ag<sub>2</sub>O clusters.<sup>(56)</sup> These impurities can adsorb Ag<sup>+</sup> ions, which then are reduced on these surfaces to Ag<sup>0</sup>, leading to a polydisperse sample with a range of particle compositions.<sup>(57)</sup> Thus, it is crucial to co-reduce the silver and palladium at similar rates into ideal PdAgNPs as efficiently as possible. Miscibility should not be an obstacle, as silver and palladium are completely miscible at all compositions.<sup>(58)</sup>

Optimization was done by adapting synthesis methods from previous work with the goal of creating highly monodisperse ( $\sigma < \pm 20\%$ ) nanoparticles with approximately 1:1 Pd to Ag.<sup>(17; 47)</sup> Initially, the metal precursors, K<sub>2</sub>PdCl<sub>4</sub> and AgNO<sub>3</sub>, were dissolved separately in ethylene glycol (EG) before being injected at a controlled rate via syringe pump into an EG solution of *poly*(vinylpyrrolidone) (PVP) and sodium borohydride (NaBH<sub>4</sub>) held at 150 °C. Two precursor injection rates were

used to determine the effect, if any, of injection rate on NP formation,  $300 \text{ cm}^3 \text{ h}^{-1}$  ( $6.0 \text{ mmol h}^{-1}$ ) and  $150 \text{ cm}^3 \text{ h}^{-1}$  ( $3.0 \text{ mmol h}^{-1}$ ) (Figure 3.1). Controlling the precursor injection rate controls the rate at which the reaction solution reaches supersaturation, which initiates nucleation of small nanoparticle clusters.<sup>(52)</sup> Variation of the injection rate led to negligible changes in size distribution, likely due to both injection rates promptly reaching supersaturation and thus leading to nucleation. Using an injection rate of  $300 \text{ cm}^3 \text{ h}^{-1}$  yielded  $9.78 \pm 4.21 \text{ nm}$  nanoparticles ( $\sigma = \pm 43.0\%$ ), while  $150 \text{ cm}^3 \text{ h}^{-1}$  yielded  $9.23 \pm 4.72 \text{ nm}$  nanoparticles ( $\sigma = \pm 51.1\%$ ).

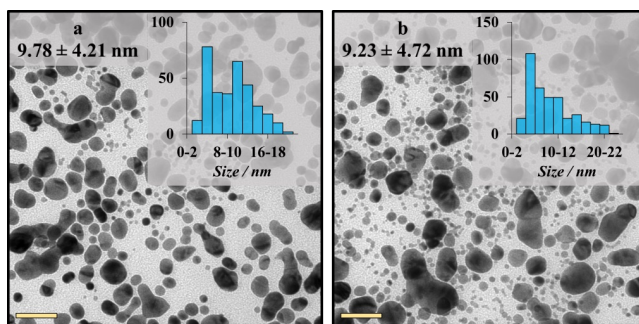


**Figure 3.1:** TEM images comparing precursor injection rates for optimization without an external reducing agent. a) A pump rate of  $300 \text{ cm}^3 \text{ h}^{-1}$ . b) A pump rate of  $150 \text{ cm}^3 \text{ h}^{-1}$ .

The use of an external reducing agent was studied by adding  $\text{NaBH}_4$  in a 1:1 molar ratio with Pd precursor for different reaction times  $t$  (Figure 3.2). A strong external reducing agent accelerates the reduction rates of both ionic precursors,  $\text{Pd}^{2+}$  and  $\text{Ag}^+$ , so that both metals nucleate at similar rates, hopefully leading to randomly alloyed, monodisperse 1:1 nanoparticles. The use of  $\text{NaBH}_4$  as the external reducing agent did impart higher monodispersity as the reaction time  $t$  increased from 2 to 5 to 10 minutes. At  $t$  equal to 2 minutes, synthesis yielded nanoparticles of  $11.34$

$\pm 2.65$  nm ( $\sigma = \pm 23.4\%$ ). Extending  $t$  to 10 minutes produced particles of  $5.53 \pm 0.90$  nm ( $\sigma = \pm 16.3\%$ ). However, attempts to repeat this synthesis were met with failure (Figure A.2). In addition to yielding nanoparticles with a range of

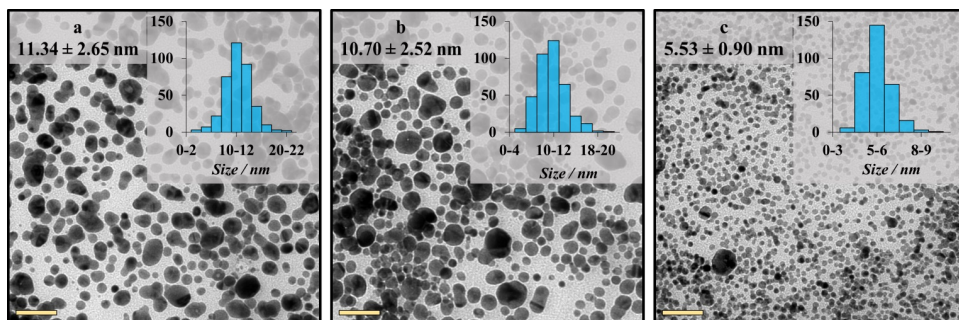


**Figure 3.2:** TEM images comparing reaction times  $t$  with the use of an external reducing agent,  $\text{NaBH}_4$ . All reactions done with a precursor injection rate of  $300 \text{ cm}^3 \text{ h}^{-1}$ . a)  $t$  being 2 min. b)  $t$  being 5 min. c)  $t$  being 10 min.

diameters, the use of  $\text{K}_2\text{PdCl}_4$  as the palladium precursor also led to the formation of  $\text{AgCl}$ . This presented several problems, including heterogeneous nucleation sites (as discussed above) and the loss of silver from the alloy. This loss of silver shifted the composition of the nanoparticles from a 1:1 Pd:Ag alloy to higher ratios as evidenced by the shift of the X-ray diffraction peaks toward pure palladium (Figure A.3).

To simplify the synthesis, the palladium precursor was changed to  $\text{Pd}(\text{NO}_3)_2$ , and the external reducing agent,  $\text{NaBH}_4$ , was excluded. By changing the counter ion of the palladium to  $\text{NO}_3^-$ , the formation of silver salt by-products (e.g.,  $\text{AgCl}$ ) was eliminated. However, it was found that the presence of  $\text{NO}_3^-$  as the counter-ion in ethylene glycol accelerated the rate of palladium reduction. This increase in reduction rate led to irregular nanoparticle growth, as the  $\text{Pd}^{2+}$  was reduced to metallic  $\text{Pd}^0$  at room temperature before being injected into the  $\mu\text{wI}$ -heated reaction vessel. To combat this issue, the presolvent for both metal precursors was changed

to water, where the reduction of  $\text{Pd}^{2+}$  to  $\text{Pd}^0$  does not occur as quickly as in ethylene glycol. This prevented premature nucleation of the metals; it also allowed both metal salts to be dissolved together in  $5 \text{ cm}^3$  of water. The synthesis of the nanoparticles was then performed by injecting the Pd-Ag/ $\text{H}_2\text{O}$  solution into the hot PVP/EG solution at a rate of  $300 \text{ cm}^3 \text{ h}^{-1}$ . Two different concentrations of PVP capping agent were tested (Figure 3.3). Initially, 2 molar equivalence (per mole of total metal, i.e. Pd + Ag) of PVP capping agent was used. This yielded large, irregularly shaped particles with a wide size distribution. Analysis of the particles gave a particle size of  $6.58 \pm 2.66 \text{ nm}$  ( $\sigma = \pm 40.4\%$ ). When the amount of PVP was increased to 5 molar equivalence, the shape of the synthesized particles become more uniform, and the size became more monodisperse. TEM analysis showed nanoparticles of  $5.97 \pm 1.14 \text{ nm}$  ( $\sigma = \pm 19.1\%$ ). Additionally, powder X-ray diffraction analysis indicated nanoparticle composition close to the targeted 1:1 ratio (Figure A.3).

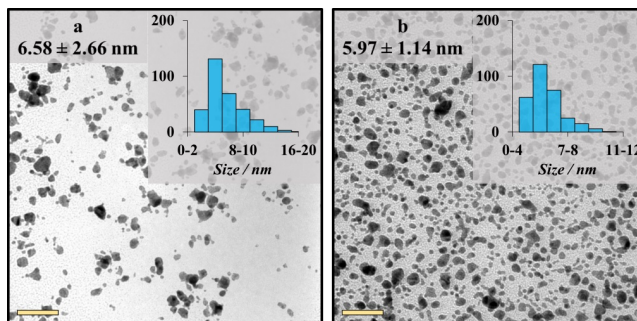


**Figure 3.3:** TEM images of PdAgNPs synthesized using  $\text{Pd}(\text{NO}_3)_2$  and  $\text{AgNO}_3$  with different equivalences of PVP (equiv per mmol total metal). a) 2.0 equiv. b) 5.0 equiv.

From the optimization process, it was concluded that the ideal synthesis of  $\text{Pd}_X\text{Ag}_{100-X}$ NPs was performed by simultaneously dissolving  $\text{Pd}(\text{NO}_3)_2$  and  $\text{AgNO}_3$

in 5 cm<sup>3</sup> deionized water. This precursor solution was then added at a rate of 300 cm<sup>3</sup> h<sup>-1</sup> to a 5 molar equivalent (per mole of total metal) PVP/EG solution that was pre-heated to 150 °C. These conditions afforded monodisperse nanoparticles that demonstrated a high degree of bulk alloying between palladium and silver.

### 3.2 Synthesis of Pd<sub>X</sub>Ag<sub>100-X</sub>NPs ( $X = 50-100$ )

The above optimized synthesis was then applied to create a suite of randomly alloyed Pd<sub>X</sub>Ag<sub>100-X</sub>NPs, where “X” represents the molar percent of palladium in the alloy. Initial attempts to synthesize nanoparticles with palladium compositions under 50% led to agglomeration and non-uniform particles ([Figure A.4](#)). Additionally, previous work studying alloys of catalytically active metals (e.g., Pd and Rh) and catalytically inactive metals (e.g., Au and Ag) has shown that nanoparticles with small ratios of catalytically active metals exhibit little to no catalytic activity themselves.<sup>(17; 47; 48)</sup> From these results, the lower limit for  $X$  was set at 50%, with Pd percentage targets of 50, 60, 70, 80, 90, and 100. It was assumed that the value of  $X$  would be regulated only by the relative molar amounts of palladium and silver salts, and the total molar amount of palladium and silver was kept constant in each reaction. For all Pd<sub>X</sub>Ag<sub>100-X</sub>NPs, the reaction conditions were identical to those described above. For pure PdNPs, the precursor salt used was K<sub>2</sub>PdCl<sub>4</sub>, and the concentration of PVP was increased to 20 equivalents; all conditions were otherwise identical. The targeted theoretical and measured values of  $X$  are shown in [Table 3.1](#). Results from ICP-OES analysis shows that the actual Pd:Ag molar ratios closely agree with the targeted compositions. The metal (Pd + Ag) mass loading on the

**Table 3.1:** Average composition values of PdAgNPs

target molar %		actual molar % <sup>α</sup>		mass % <sup>α</sup>	
Pd	Ag	Pd	Ag	Pd	Ag
100	0	100	0	1.38	0.00
90	10	95	5	1.38	0.07
80	20	81	19	1.29	0.31
70	30	72	28	1.22	0.46
60	40	63	37	0.99	0.60
50	50	51	49	0.73	0.71

<sup>α</sup>Based on ICP-OES analysis of am-SiO<sub>2</sub> supported PdAgNPs.

am-SiO<sub>2</sub> was between 1.3% and 1.7% for all catalysts (column 3, Table 3.1).

The synthesized Pd<sub>X</sub>Ag<sub>100-X</sub>NPs had average diameters ranging from 3.6 to 6.0 nm, with each composition showing good monodispersity ( $\sigma < \pm 20\%$ ) (Figure 3.4). The nanoparticle size tended to gradually decrease for more Pd rich nanoparticles, a trend in direct contrast to previous work looking at alloyed PdAuNPs.<sup>(17; 47)</sup> Additionally, not all of the alloyed nanoparticles are smaller than the synthesized pure PdNPs. One possible explanation is due to the two-stage formation of PdAgNPs, similar to that of PdAuNPs.<sup>(47; 59)</sup> First, PdNPs are formed from reduced Pd<sup>0</sup> atoms. Secondly, Ag<sup>+</sup> is autocatalytically reduced by Pd<sup>0</sup> to Ag<sup>0</sup> atoms that diffuse into the PdNPs, creating the alloyed PdAgNPs. This process is further accelerated by hydroxyl radicals (OH·) from water in the system. As the overall silver content increases, more Ag<sup>0</sup> atoms diffuse into the NPs, thus leading to larger NP diameters. TEM analysis also reveals a majority of truncated octahedron-shaped particles. Truncated octahedron particles represent the equilibrium shape for face-centered cubic (FCC) nanoparticles.<sup>(60; 61; 62; 63)</sup> Additionally, the truncated octahedral surface consists of mostly {111} and {100} facets with corresponding edges, which is im-

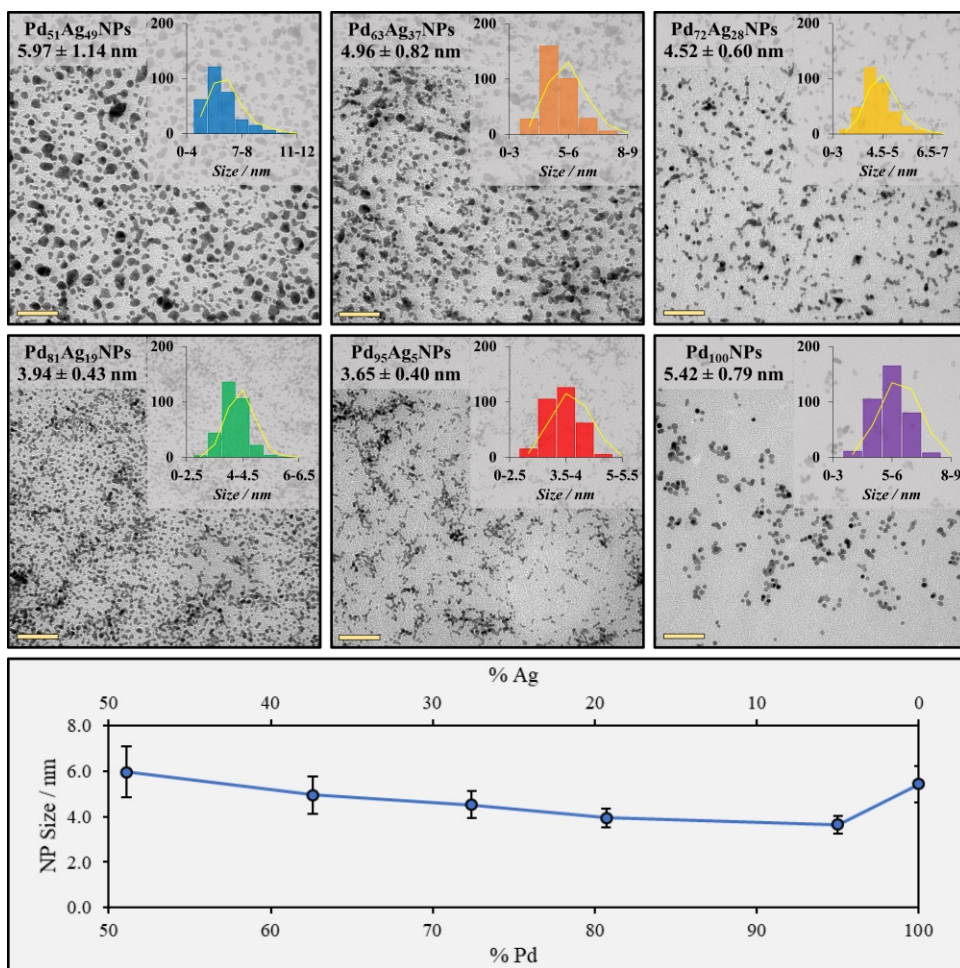


**Figure 3.4:** Representative TEM images showing  $\text{Pd}_x\text{Ag}_{100-x}$  NPs. Inset are the size distributions for each composition with associated histograms of measured sizes. Scale bars are 50 nm.

portant as  $\{100\}$  facets have been shown to be the most active for aqueous  $\text{NO}_2^-$  reduction.<sup>(42)</sup>

Powder X-ray diffraction (PXRD) analysis was used to assess random alloying in the bulk for each batch of nanoparticles. Assuming a FCC lattice for both pure Pd and pure Ag, the alloyed nanoparticles should also show FCC lattice structures

with shifts in the Bragg reflections that correspond to the molar composition of each alloy; this shift can be seen in Figure 3.5 (and further in Figure A.5). The observed

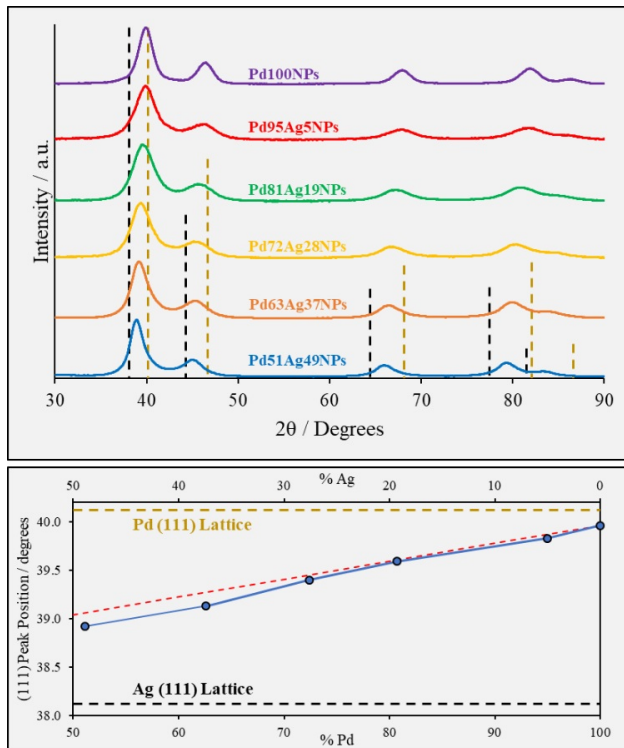


**Figure 3.5:** PXRD patterns for  $\text{Pd}_X\text{Ag}_{100-X}\text{NPs}$  (top). Comparison of (111) Bragg reflection as a function of composition (bottom). Dashed lines are reference peaks (shown with relative intensities) for pure palladium (gold) and pure silver (black). The dashed red line indicates calculated values for the (111) reflection.

maxima for the (111) reflection shifts from  $2\theta_{\max} = 39.960^\circ$  for pure PdNPs (pure Pd, expected  $40.1^\circ$ ) to lower angles as the percentage of Ag increased (pure Ag, expected  $38.1^\circ$ ). For  $\text{Pd}_{51}\text{Ag}_{49}\text{NPs}$ , the observed (111) reflection appears at  $2\theta_{\max} = 38.920^\circ$ ; this value closely agrees with the calculated value of  $39.0^\circ$  assuming  $\text{Pd}_{50}\text{Ag}_{50}\text{NPs}$  with FCC lattice structure. No additional peaks that could represent either pure palladium or pure silver phase were observed. Similarly for  $\text{Pd}_{95}\text{Ag}_5\text{NPs}$ ,

the observed (111) reflection of  $2\theta_{\max} = 39.830^\circ$  closely agrees with calculated value of  $39.8^\circ$  for Pd<sub>90</sub>Ag<sub>10</sub>NPs. Thus PXRD indicates bulk alloying of palladium and silver in the nanoparticles across all compositions. Random alloying of the nanoparticles was also supported via HR-TEM and 2D-EDS mapping of individual Pd<sub>95</sub>Ag<sub>5</sub>NPs (Figure 3.6). Calculation of the lattice spacing using high resolution TEM images

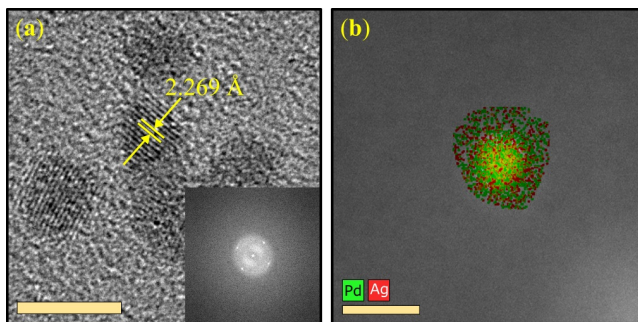


**Figure 3.6:** (a) HR-TEM image of a synthesized Pd<sub>95</sub>Ag<sub>5</sub>NP showing the d lattice spacing of 2.269 Å; inset shows the fast Fourier transform (FFT). (b) 2D-EDS image of a single Pd<sub>95</sub>Ag<sub>5</sub>NP showing the elemental mapping of Pd and Ag atoms. The scale bars for both images are 5 nm.

resulted in a d lattice spacing of 2.269 Å between  $\langle 111 \rangle$  planes for Pd<sub>95</sub>Ag<sub>5</sub>NPs, which closely agrees with the calculated spacing of 2.252 Å based on a weighted average of pure Pd  $\langle 111 \rangle$  and pure Ag  $\langle 111 \rangle$  lattice spacings (2.246 Å and 2.359 Å, respectively). Additionally, elemental mapping from 2D-EDS shows no evidence of metal segregation in the nanoparticles, indicating random alloying.

### 3.3 Catalyst Performance and Recyclability

The synthesized Pd<sub>X</sub>Ag<sub>100-X</sub>NPs were then supported on amorphous silica for use as NO<sub>2</sub><sup>-</sup> reduction catalysts; total metal loading rates (Pd + Ag) are shown above in Table 3.1. Pseudo-first-order kinetics were observed for NO<sub>2</sub><sup>-</sup> reduction using all

catalysts. Apparent first-order rates were determined from  $\text{NO}_2^-$  concentration plots, before being normalized to the total metal loading of each catalyst (Figure 3.7). The catalytic activity showed an increasing trend as the molar ratio became more

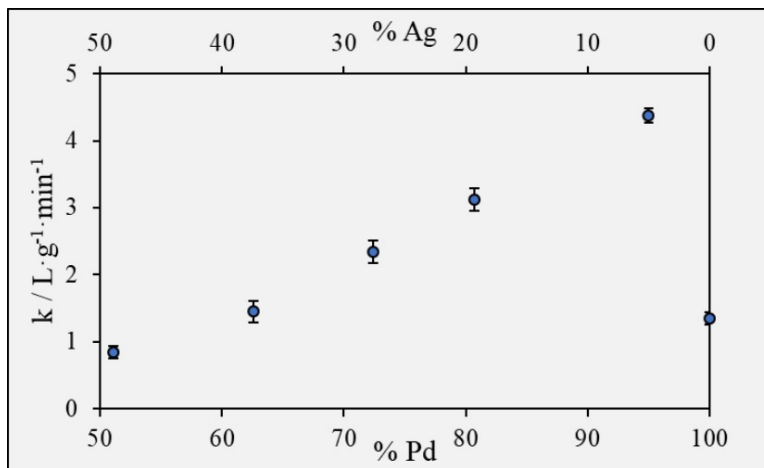


**Figure 3.7:** Total metal mass normalized first-order rate constants for PdAgNP-SiO<sub>2</sub> catalysts.

palladium-rich. The peak activity was observed for Pd<sub>95</sub>Ag<sub>5</sub>NPs, though nearly all compositions displayed activities greater than that of pure PdNPs supported on silica even though silver is catalytically inactive for  $\text{NO}_2^-$  reduction on its own. The calculated rate constant for the Pd<sub>95</sub>Ag<sub>5</sub>NP-SiO<sub>2</sub> catalyst was 4.38 L g<sub>metal</sub><sup>-1</sup> min<sup>-1</sup>. The measured rate constant for PdNP-SiO<sub>2</sub> catalyst was 1.35 L g<sub>metal</sub><sup>-1</sup> min<sup>-1</sup>. Previous work looking at alloyed PdAuNPs found a similar relationship between the  $\text{NO}_2^-$  reduction activity levels of alloyed and pure NP catalysts; Seraj and co-workers reported a maximum rate constant of 5.12 L g<sub>metal</sub><sup>-1</sup> min<sup>-1</sup> for the highest performing PdAuNP catalyst. However, this maximum activity was reported for nanoparticles with a Pd-to-Au ratio of 53:47, a much lower palladium content than in Pd<sub>95</sub>Ag<sub>5</sub>NPs. Additionally, the increase in  $\text{NO}_2^-$  reduction rate from alloying Au with Pd was found

to be around 250%, which is slightly less than the improvement (320% increase) seen from alloying Ag and Pd.<sup>(17)</sup> For all catalysts, the selectivity of  $\text{NO}_2^-$  reduction to  $\text{N}_2$  gas was greater than 98%, including pure PdNPs, as shown in [Table 3.2](#). Previously reported values of  $\text{N}_2$  selectivity using Pd-based catalysts for  $\text{NO}_2^-$  reduction support these findings.<sup>(17; 28; 32)</sup>

**Table 3.2:** Nitrite reduction selectivity of various  $\text{SiO}_2$ -supported PdAgNPs

% Pd	% Ag	% $\text{N}_2$
100	0	98.7
95	5	>99.9
81	19	>99.9
72	28	99.4
63	37	99.4
51	49	98.5

The results found here, that more Pd-rich catalysts outperform pure PdNPs, is similar to previous work looking at alloyed RhAgNPs for gas-phase cyclohexene hydrogenation.<sup>(48)</sup> This could be due to the fact that the rate limiting step in both aqueous reactions and gas-phase reactions may be similar. Previous DFT calculations show that while catalytically active metals, such as palladium and rhodium, rapidly undergo oxidative  $\text{H}_2$  addition, the resulting adsorbed H atoms are strongly bound. However, catalytically inactive metals, such as silver or gold, are unable to cleave  $\text{H}_2$  on their own and can only weakly bind already activated H atoms.<sup>(47; 48)</sup> Thus, while H migration and end-product desorption is slow for pure PdNP or pure RhNP catalysts, the integration of Ag or Au into the catalyst can lower the binding energy, resulting in faster desorption of hydrogenated products. It is not unreasonable to assume similar reasoning can be applied to the catalytic reduction of aqueous-phase

$\text{NO}_2^-$  using the synthesized PdAgNP-SiO<sub>2</sub> catalysts here.

Palladium is a precious metal, with a current market price of around \$44 per gram (APMEX, Inc; May 2019), and represents a major fraction of the overall costs for catalytic treatment systems.<sup>(23)</sup> The price of silver, though, is a fraction of that of palladium, at \$0.48 per gram (APMEX, Inc; May 2019); thus, it is important to also pay attention to the activity per cost of each PdAgNP-SiO<sub>2</sub> catalyst. Assuming the costs for each catalyst comes mainly from the metals needed for the nanoparticles, the observed first-order rate constants can be normalized to the dollar costs of the catalysts (Table B.1). The calculated rate constants again peaked for the Pd<sub>95</sub>Ag<sub>5</sub>NP-SiO<sub>2</sub> catalyst (0.104 L min<sup>-1</sup> USD<sup>-1</sup>). However, all alloyed catalysts outperformed the pure PdNP-SiO<sub>2</sub> catalyst (0.0307 L min<sup>-1</sup> USD<sup>-1</sup>). The results show that alloying silver into the NP catalysts represents a valid option for lowering the catalyst cost while maintaining, or even enhancing, catalyst activity for  $\text{NO}_2^-$  reduction.

The use of palladium for widespread water treatment is also hindered over concerns of natural supply limits.<sup>(19)</sup> The implementation of a precious metal-based catalyst system for water treatment is reliant on its subsequent activity through repeated catalyst cycles over the course of months or years of operation. To investigate the longevity of the PdAgNP catalysts, Pd<sub>95</sub>Ag<sub>5</sub>NP-SiO<sub>2</sub> and pure PdNP-SiO<sub>2</sub> catalysts were each subjected to repeated  $\text{NO}_2^-$  reduction cycles in batch systems. The total metal normalized rate constants were calculated for each cycle (Figure 3.8). Initially, the activities of both catalysts closely agreed with those measured in single-run, batch reactor experiments (4.46 L g<sub>metal</sub><sup>-1</sup> min<sup>-1</sup> and 1.65 L g<sub>metal</sub><sup>-1</sup> min<sup>-1</sup>

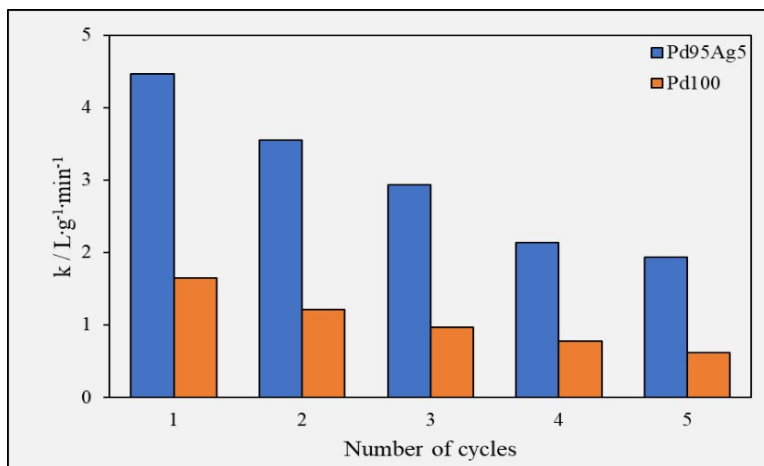


**Figure 3.8:** Catalytic activity comparison between Pd<sub>95</sub>Ag<sub>5</sub>NP-SiO<sub>2</sub> catalyst (blue) and pure PdNP-SiO<sub>2</sub> catalyst (orange) with multiple cycles of NO<sub>2</sub><sup>-</sup> reduction.

for Pd<sub>95</sub>Ag<sub>5</sub>NP-SiO<sub>2</sub> and PdNP-SiO<sub>2</sub>, respectively). With each repeated catalytic cycle, the activities decreased. Both catalysts displayed similar patterns of activity loss with each cycle (Table B.2). After 5 cycles, the Pd<sub>95</sub>Ag<sub>5</sub>NP-SiO<sub>2</sub> catalyst maintained 43% of its original activity, as compared to 37% for the pure PdNP-SiO<sub>2</sub> catalyst, and despite the loss in activity, the Pd<sub>95</sub>Ag<sub>5</sub>NP-SiO<sub>2</sub> catalyst displayed higher activity than new, unused PdNP-SiO<sub>2</sub> catalyst. After completing multiple NO<sub>2</sub><sup>-</sup> reduction cycles, the nanoparticle catalysts were characterized to analyze possible deactivation mechanisms. PXRD analysis of the Pd<sub>95</sub>Ag<sub>5</sub>NP-SiO<sub>2</sub> catalyst showed no noticeable metal segregation, indicating that the majority of the nanoparticles remained randomly alloyed (Figure B.2). Additionally, TEM revealed that the nanoparticles underwent no appreciable agglomeration throughout repeated reduction cycles (Figure B.3). Post-recycling ICP-OES analysis revealed no measurable changes in weight percent metal loadings of the two catalysts, thus indicating that metal leaching from the catalysts was not occurring. From the complementary characterization, it is clear

that measurable physical changes (e.g., de-alloying, agglomeration, dissolution) are not responsible for the observed loss of catalyst activity. However, it is unclear at this time if segregation of the metals, specifically migration of either palladium or silver to the nanoparticle surface, is occurring and limiting subsequent  $\text{NO}_2^-$  reduction.

## Chapter 4: Conclusions and Future Work

Palladium is a rare, noble metal that represents a significant portion of the overall costs for catalytic water treatment, costing around \$44 per gram (APMEX, Inc; May 2019). Silver, at \$0.48 per gram (APMEX, Inc; May 2019), is a fraction of the cost. The incorporation of silver into bimetallic, alloyed nanoparticles presents a possible route for improving the performance of catalysts while also lowering the costs. Microwave-assisted heating can be used to synthesize monodisperse, randomly alloyed PdAgNPs with controlled composition tuning. Moreover, these PdAgNP catalysts display considerably higher activity for  $\text{NO}_2^-$  reduction than pure PdNP catalysts when supported on amorphous silica. The results also indicate, though, that the alloyed PdAgNP catalysts lose activity with repeated use, similar to pure PdNP catalysts. However, further work is needed to explore the mechanism for this catalyst deactivation in order to improve catalyst design to ensure that catalytic activity is maintained with long-term use.

Additional work is also needed to explore the use of different transition metal oxide support materials to better understand how these materials may affect catalytic activity and selectivity of randomly alloyed bimetallic nanoparticles for aqueous  $\text{NO}_2^-$  reduction. It is possible that strong metal-support interactions (SMSI) between these alloyed nanoparticles and oxide supports can increase hydrogenation rates of aqueous  $\text{NO}_2^-$ , similar to the gas-phase hydrogenation of carbon monoxide (CO) to methane ( $\text{CH}_4$ ).<sup>(64)</sup> Additionally, these transition metal oxides may provide for

hydrogen spillover from the nanoparticles to the surrounding oxide support, thus increasing the concentration of activated hydrogen on the catalyst surface.<sup>(65; 66)</sup> Controlling the amount of spilled over hydrogen could lead to an enhancement of  $\text{NO}_2^-$  reduction rates or could lend more control over the  $\text{N}_2:\text{NH}_4^+$  ratio of end products. It is also unknown how incorporation of promoter metals, such as copper or indium, will affect alloyed nanoparticles. Future studies are needed to discover whether the trends in activity versus particle composition seen in  $\text{NO}_2^-$  reduction remain the same for  $\text{NO}_3^-$  reduction with a promoter metal. Lastly, further insight into the reduction mechanisms, through both experimental and theoretical modeling, is needed to determine how factors such as catalyst composition, catalyst metal loading, and catalyst–promoter–support interactions can be used to optimise catalyst design for  $\text{NO}_3^-$  and  $\text{NO}_2^-$  reduction in water treatment systems.

# Appendices

## A Nanoparticle Optimization, Synthesis, and Characterization

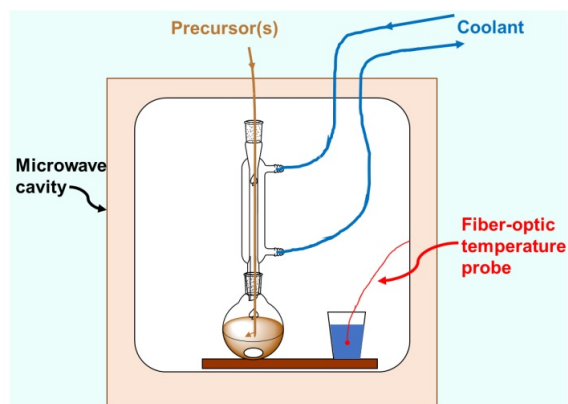


Figure A.1: Microwave set-up used for nanoparticle synthesis reactions.

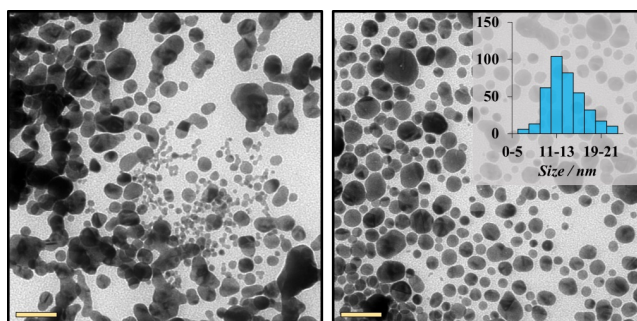
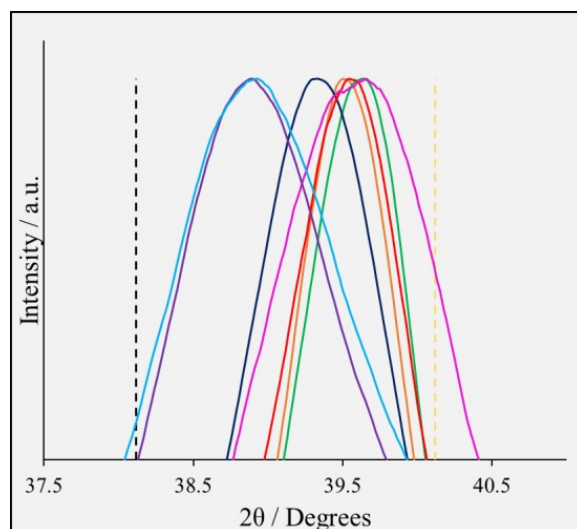
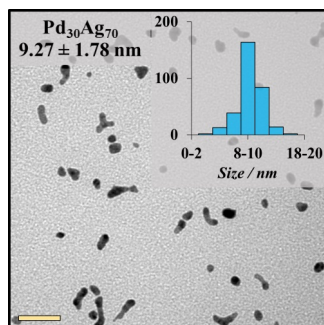


Figure A.2: TEM images of attempts to replicate PdAgNP synthesis using an injection rate of  $300 \text{ cm}^3 \text{ h}^{-1}$ ,  $\text{NaBH}_4$  as a external reducing agent, and a reaction time  $t$  of 10 minutes.



**Figure A.3:** Powder X-ray diffraction patterns showing the (111) peak of attempts to optimize the synthetic process for PdAgNPs. The orange and green spectra correspond to injection rate optimization ( $300$  and  $150 \text{ cm}^3 \text{ h}^{-1}$ , respectively); dark blue, red, and pink to reactions done with  $\text{NaBH}_4$  ( $t$  of 2 min, 5 min, 10 min, respectively); purple and light blue to reactions with  $\text{Pd}(\text{NO}_3)_2$  (2.0 and 5.0 equiv of PVP, respectively).



**Figure A.4:** TEM image of the synthesis of a Pd-poor PdAgNP. Here, the target molar percent of palladium is 30. The measured nanoparticle size is  $9.27 \pm 1.78 \text{ nm}$  ( $\sigma = \pm 19.2\%$ ).

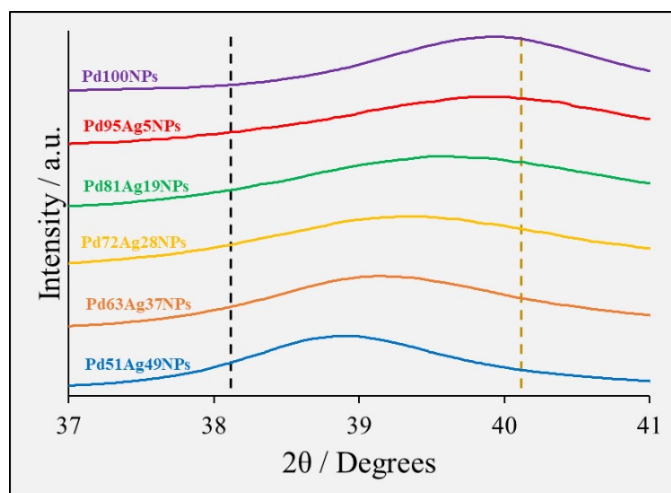


**Figure A.5:** PXRD patterns showing the shifting of the (111) Bragg reflection with respect to composition. The dashed lines are reference peak positions for pure Pd (gold) and pure Ag (black).

## B Catalyst Performance

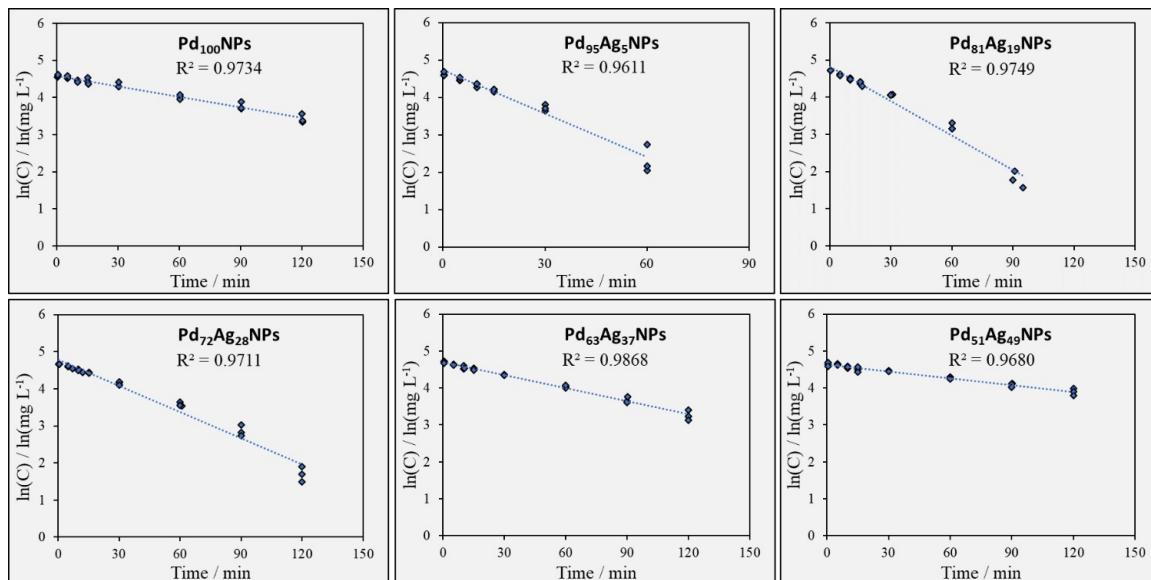


**Figure B.1:** *Log*  $\text{NO}_2^-$  concentration vs. time curves for PdAgNP-SiO<sub>2</sub> catalyzed reduction reactions. Catalysis reactions were performed in triplicate for each catalyst composition.

**Table B.1:** Pseudo-first-order rate constants for  $\text{NO}_2^-$  reduction normalized to the total cost of metal used per catalyst.

% Pd	% Ag	$k^\alpha$ L min <sup>-1</sup> USD <sup>-1</sup>
100	0	0.0368
95	5	0.0520
81	19	0.0726
72	28	0.0870
63	37	0.1040
51	49	0.0308

<sup>α</sup>Assuming a batch reactor volume of 40 cm<sup>3</sup> amended with 0.020 g of supported catalyst.

**Table B.2:** Catalyst activities over repeated  $\text{NO}_2^-$  reduction cycles.

Run	$\text{Pd}_{95}\text{Ag}_5\text{NP-SiO}_2$		$\text{PdNP-SiO}_2$	
	k $\text{L g}^{-1} \text{min}^{-1}$	% Original Activity	k $\text{L g}^{-1} \text{min}^{-1}$	% Original Activity
1	4.47	100	1.65	100
2	3.55	80	1.22	74
3	2.93	66	0.97	59
4	2.14	48	0.78	47
5	1.93	43	0.62	37

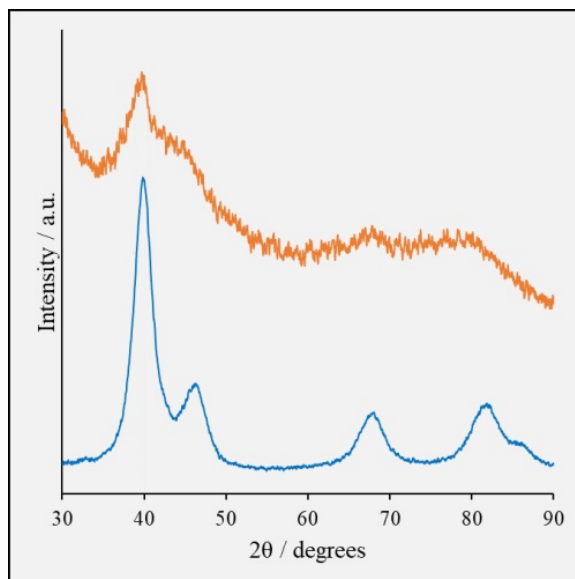


**Figure B.2:** PXRD spectra comparing  $\text{Pd}_{95}\text{Ag}_5\text{NPs}$  before (blue) and after (orange) multiple  $\text{NO}_2^-$  reduction cycles.

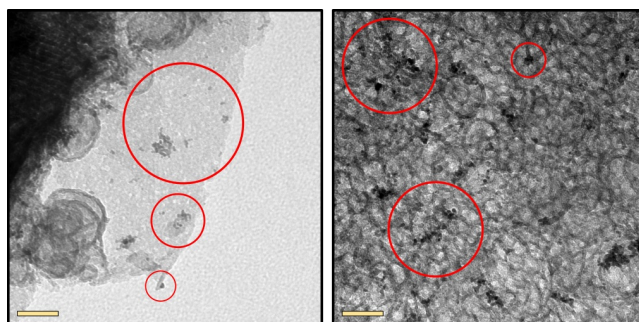


**Figure B.3:** TEM images of SiO<sub>2</sub>-supported Pd<sub>95</sub>Ag<sub>5</sub>NPs before (left) and after (right) multiple NO<sub>2</sub><sup>-</sup> reduction cycles. The red circles are to help differentiate nanoparticles from the amorphous silica support.

## Bibliography

- [1] “Water–Energy Nexus: Challenges and Opportunities,” 2015.
- [2] Y. B. Yin, S. Guo, K. N. Heck, C. A. Clark, C. L. Coonrod, and M. S. Wong, “Treating Water by Degrading Oxyanions Using Metallic Nanostructures,” *ACS Sustainable Chemistry and Engineering*, vol. 6, no. 9, pp. 11160–11175, 2018.
- [3] A. Liu, J. Ming, and R. O. Ankumah, “Nitrate Contamination in Private Wells in Rural Alabama, United States,” *Science of the Total Environment*, vol. 346, no. 1-3, pp. 112–120, 2005.
- [4] L. Fewtrell, “Drinking-Water Nitrate, Methemoglobinemia, and Global Burden of Disease: A Discussion,” *Environmental Health Perspectives*, vol. 112, no. 14, pp. 1371–1374, 2004.
- [5] A. R. Townsend, R. W. Howarth, F. A. Bazzaz, M. S. Booth, C. C. Cleveland, S. K. Collinge, A. P. Dobson, P. R. Epstein, E. A. Holland, D. R. Keeney, M. A. Mallin, C. A. Rogers, P. Wayne, and A. H. Wolfe, “Human Health Effects of a Changing Nitrogen Cycle,” *Frontiers in Ecology and the Environment*, vol. 1, no. 5, pp. 240–246, 2003.
- [6] R. L. Seiler, “Combined Use of  $^{15}\text{N}$  and  $^{18}\text{O}$  of Nitrate and  $^{11}\text{B}$  to Evaluate

- Nitrate Contamination in Groundwater,” *Applied Geochemistry*, vol. 20, no. 9, pp. 1626–1636, 2005.
- [7] P. J. Weyer, J. R. Cerhan, B. C. Kross, G. R. Hallberg, J. Kantamneni, G. Breuer, M. P. Jones, W. Zheng, and C. F. Lynch, “Municipal Drinking Water Nitrate Level and Cancer Risk in Older Women: The Iowa Women’s Health Study,” *Epidemiology*, vol. 12, no. 3, pp. 327–338, 2001.
- [8] S. M. A. Adelana, “Nitrate Health Effects,” *Water Encyclopedia*, vol. 3, no. 3, 2005.
- [9] K. R. Burow, B. T. Nolan, M. G. Rupert, and N. M. Dubrovsky, “Nitrate in Groundwater of the United States, 1991–2003,” *Environmental Science and Technology*, vol. 44, no. 13, pp. 4988–4997, 2010.
- [10] P. J. Squillace, J. C. Scott, M. J. Moran, B. T. Nolan, and D. W. Kolpin, “VOCs, Pesticides, Nitrate, and Their Mixtures in Groundwater Used for Drinking Water in the United States,” *Environmental Science and Technology*, vol. 36, no. 9, pp. 1923–1930, 2002.
- [11] M. Maupin, J. Kenny, S. Hutson, J. K. Lovelace, N. Barber, and K. Linsey, “Estimated Use of Water in the United States in 2010: Circular 1405,” 2010.
- [12] B. T. Nolan and J. D. Stoner, “Nutrients in Groundwaters of the Conterminous United States, 1992–1995,” *Environmental Science and Technology*, vol. 34, no. 7, pp. 1156–1165, 2000.

- [13] P. F. Hudak, "Regional Trends in Nitrate Content of Texas Groundwater," *Journal of Hydrology*, vol. 228, no. 1-2, pp. 37–47, 2000.
- [14] A. Kapoor and T. Viraraghavan, "Nitrate Removal From Drinking Water – Review," *Journal of Environmental Engineering*, vol. 123, no. 4, pp. 371–380, 1997.
- [15] E. Elisante and A. N. N. Muzuka, "Occurrence of Nitrate in Tanzanian Groundwater Aquifers: A Review," *Applied Water Science*, vol. 7, no. 1, pp. 71–87, 2017.
- [16] J. Wu and Z. Sun, "Evaluation of Shallow Groundwater Contamination and Associated Human Health Risk in an Alluvial Plain Impacted by Agricultural and Industrial Activities, Mid-west China," *Exposure and Health*, vol. 8, no. 3, pp. 311–329, 2016.
- [17] S. Seraj, P. Kunal, H. Li, G. Henkelman, S. M. Humphrey, and C. J. Werth, "PdAu Alloy Nanoparticle Catalysts: Effective Candidates for Nitrite Reduction in Water," *ACS Catalysis*, vol. 7, no. 5, pp. 3268–3276, 2017.
- [18] L. Wang, A. S. C. Chen, A. Wang, and W. E. Condit, "Arsenic and Nitrate Removal from Drinking Water by Ion Exchange: U.S. EPA Demonstration Project at Vale, OR. Final Performance Evaluation Report," Tech. Rep. April, U.S. EPA, 2011.
- [19] J. K. Choe, A. M. Bergquist, S. Jeong, J. S. Guest, C. J. Werth, and T. J. Strathmann, "Performance and Life Cycle Environmental Benefits of Recycling

- Spent Ion Exchange Brines by Catalytic Treatment of Nitrate,” *Water Research*, vol. 80, pp. 267–280, 2015.
- [20] S. G. Lehman, M. Badruzzaman, S. Adham, D. J. Roberts, and D. A. Clifford, “Perchlorate and Nitrate Treatment by Ion Exchange Integrated with Biological Brine Treatment,” *Water Research*, vol. 42, no. 4-5, pp. 969–976, 2008.
- [21] M. C. Ziv-El and B. E. Rittmann, “Systematic Evaluation of Nitrate and Perchlorate Bioreduction Kinetics in Groundwater using a Hydrogen-Based Membrane Biofilm Reactor,” *Water Research*, vol. 43, no. 1, pp. 173–181, 2009.
- [22] B. P. Chaplin, M. Reinhard, W. F. Schneider, C. Schüth, J. R. Shapley, T. J. Strathmann, and C. J. Werth, “Critical Review of Pd-Based Catalytic Treatment of Priority Contaminants in Water,” *Environmental Science and Technology*, vol. 46, no. 7, pp. 3655–3670, 2012.
- [23] A. M. Bergquist, J. K. Choe, T. J. Strathmann, and C. J. Werth, “Evaluation of a Hybrid Ion Exchange-Catalyst Treatment Technology for Nitrate Removal from Drinking Water,” *Water Research*, vol. 96, pp. 177–187, 2016.
- [24] R. Zhang, D. Shuai, K. A. Guy, J. R. Shapley, T. J. Strathmann, and C. J. Werth, “Elucidation of Nitrate Reduction Mechanisms on a Pd-In Bimetallic Catalyst using Isotope Labeled Nitrogen Species,” *ChemCatChem*, vol. 5, no. 1, pp. 313–321, 2013.
- [25] S. Guo, K. Heck, S. Kasiraju, H. Qian, Z. Zhao, L. C. Grabow, T. Miller, and

- M. S. Wong, “Insights into Nitrate Reduction over Indium-Decorated Palladium Nanoparticle Catalysts,” *ACS Catalysis*, vol. 8, pp. 503–515, 2018.
- [26] H. L. Tierney, A. E. Baber, J. R. Kitchin, and E. C. H. Sykes, “Hydrogen Dissociation and Spillover on Individual Isolated Palladium Atoms,” *Physical Review Letters*, vol. 103, pp. 1–4, 2009.
- [27] H. Shin, S. Jung, S. Bae, W. Lee, and H. Kim, “Nitrite Reduction Mechanism on a Pd Surface,” *Environmental Science and Technology*, vol. 48, no. 21, pp. 12768–12774, 2014.
- [28] U. Prüsse and K. D. Vorlop, “Supported Bimetallic Palladium Catalysts for Water-Phase Nitrate Reduction,” *Journal of Molecular Catalysis A: Chemical*, vol. 173, no. 1-2, pp. 313–328, 2001.
- [29] K. A. Guy, H. Xu, J. C. Yang, C. J. Werth, and J. R. Shapley, “Catalytic Nitrate and Nitrite Reduction with Pd-Cu/PVP Colloids in Water: Composition, Structure, and Reactivity Correlations,” *Journal of Physical Chemistry C*, vol. 113, pp. 8177–8185, 2009.
- [30] G. Strukul, R. Gavagnin, F. Pinna, E. Modafferri, S. Perathoner, G. Centi, M. Marella, and M. Tomaselli, “Use of Palladium Based Catalysts in the Hydrogenation of Nitrates in Drinking Water: From Powders to Membranes,” *Catalysis Letters*, vol. 55, pp. 139–149, 2000.
- [31] A. Pintar, M. Setinc, and J. Levec, “Hardness and Salt Effects on Catalytic

- Hydrogenation of Aqueous Nitrate Solutions,” *Journal of Catalysis*, vol. 87, pp. 72–87, 1998.
- [32] S. Hörold, K.-D. Vorlop, T. Tacke, and M. Sell, “Development of Catalysts for a Selective Nitrate and Nitrite Removal from Drinking Water,” *Catalysis Today*, vol. 17, pp. 21–30, 1993.
- [33] B. P. Chaplin, E. Roundy, K. A. Guy, J. R. Shapley, and C. J. Werth, “Effects of Natural Water Ions and Humic Acid on Catalytic Nitrate Reduction Kinetics Using an Alumina Supported Pd-Cu Catalyst,” *Environmental Science and Technology*, vol. 40, pp. 3075–3081, 2006.
- [34] B. P. Chaplin, J. R. Shapley, and C. J. Werth, “Regeneration of Sulfur-Fouled Bimetallic Pd-Based Catalysts,” *Environmental Science and Technology*, vol. 41, pp. 5491–5497, 2007.
- [35] A. Garron, K. Lázár, and F. Epron, “Characterization by Mössbauer Spectroscopy of Trimetallic Pd–Sn–Au/Al<sub>2</sub>O<sub>3</sub> and Pd–Sn–Au/SiO<sub>2</sub> Catalysts for Denitration of Drinking Water,” *Applied Catalysis B: Environmental*, vol. 65, pp. 240–248, 2006.
- [36] F. A. Marchesini, S. Irusta, C. Querini, and E. Miró, “Nitrate hydrogenation over Pt,In/Al<sub>2</sub>O<sub>3</sub> and Pt,In/SiO<sub>2</sub>. Effect of aqueous media and catalyst surface properties upon the catalytic activity,” *Catalysis Communications*, vol. 9, pp. 1021–1026, 2008.
- [37] D. Shuai, J. K. Choe, J. R. Shapley, and C. J. Werth, “Enhanced Activity and

- Selectivity of Carbon Nanofiber Supported Pd Catalysts for Nitrite Reduction,” *Environmental Science and Technology*, vol. 46, no. 5, pp. 2847–2855, 2012.
- [38] J. K. Chinthaginjala and L. Lefferts, “Support effect on selectivity of nitrite reduction in water,” *Applied Catalysis B: Environmental*, vol. 101, no. 1-2, pp. 144–149, 2010.
- [39] J. Sá, T. Berger, K. Föttinger, A. Riss, J. A. Anderson, and H. Vinek, “Can TiO<sub>2</sub> Promote the Reduction of Nitrates in Water?,” *Journal of Catalysis*, vol. 234, no. 2, pp. 282–291, 2005.
- [40] F. Epron, F. Gauthard, and J. Barbier, “Catalytic Reduction of Nitrate in Water on a Monometallic Pd/CeO<sub>2</sub> Catalyst,” *Journal of Catalysis*, vol. 206, no. 2, pp. 363–367, 2002.
- [41] K. Wada, T. Hirata, S. Hosokawa, S. Iwamoto, and M. Inoue, “Effect of Supports on Pd-Cu Bimetallic Catalysts for Nitrate and Nitrite Reduction in Water,” *Catalysis Today*, vol. 185, no. 1, pp. 81–87, 2012.
- [42] D. Shuai, D. C. Mccalman, J. K. Choe, and J. R. Shapley, “Structure Sensitivity Study of Waterborne Contaminant Hydrogenation Using Shape- and Size-Controlled Pd Nanoparticles,” *ACS Catalysis*, vol. 3, pp. 453–463, 2013.
- [43] H. Qian, Z. Zhao, J. C. Velazquez, L. A. Pretzer, N. Heck, and M. S. Wong, “Supporting palladium metal on gold nanoparticles improves its catalysis for nitrite reduction,” *Nanoscale*, vol. 6, pp. 358–364, 2014.

- [44] J. H. Sinfelt, "Catalysis by Alloys and Bimetallic Clusters," *Accounts of Chemical Research*, vol. 10, no. 5, pp. 15–20, 1977.
- [45] P. Liu and J. K. Norskov, "Ligand and ensemble effects in adsorption on alloy surfaces," *Physical Chemistry Chemical Physics*, vol. 3, no. 111, pp. 3814–3818, 2001.
- [46] M. Chen, D. Kumar, C.-w. Yi, and D. W. Goodman, "The Promotional Effect of Gold in Catalysis by Palladium-Gold," *Science*, vol. 310, no. 5746, pp. 291–294, 2005.
- [47] P. Kunal, H. Li, B. L. Dewing, L. Zhang, K. Jarvis, G. Henkelman, and S. M. Humphrey, "Microwave-Assisted Synthesis of Pd<sub>x</sub>Au<sub>100-x</sub> Alloy Nanoparticles: A Combined Experimental and Theoretical Assessment of Synthetic and Compositional Effects upon Catalytic Reactivity," *ACS Catalysis*, vol. 6, no. 8, pp. 4882–4893, 2016.
- [48] S. Garcia, L. Zhang, G. W. Piburn, G. Henkelman, and S. M. Humphrey, "Microwave Synthesis of Classically Immiscible Rhodium-Silver and Rhodium-Gold Alloy Nanoparticles: Highly Active Hydrogenation Catalysts," *ACS Nano*, no. 11, pp. 11512–11521, 2014.
- [49] J. Radnik, C. Mohr, and P. Claus, "On the origin of binding energy shifts of core levels of supported gold nanoparticles and dependence of pretreatment and material synthesis," *Physical Chemistry Chemical Physics*, vol. 5, pp. 172–177, 2003.

- [50] R. L. Vander Wal, T. M. Tichich, and V. E. Curtis, "Substrate–support interactions in metal-catalyzed carbon nanofiber growth," *Carbon*, vol. 39, pp. 2277–2289, 2001.
- [51] M. Figlarz, F. Fievet, and J.-P. Lagier, "Process for the Reduction of Metallic Compounds by Polyols, and Metallic Powders Obtained by this Process," 1985.
- [52] N. Dahal, S. García, J. Zhou, and S. M. Humphrey, "Beneficial Effects of Microwave-Assisted Heating versus Conventional Heating in Noble Metal Nanoparticle Synthesis," *ACS Nano*, vol. 6, no. 11, pp. 9433–9446, 2012.
- [53] S. García, R. M. Anderson, H. Celio, N. Dahal, A. Dolocan, J. Zhou, and S. M. Humphrey, "Microwave Synthesis of Au-Rh Core-Shell Nanoparticles and Implications of the Shell Thickness in Hydrogenation Catalysis," *Chemical Communications*, vol. 49, no. 39, pp. 4241–4243, 2013.
- [54] H. Zhang, J. Sun, D. Ma, X. Bao, A. Klein-Hoffmann, G. Weinberg, D. Su, and R. Schlögl, "Unusual Mesoporous SBA-15 with Parallel Channels Running along the Short Axis," *Journal of the American Chemical Society*, vol. 126, no. 24, pp. 7440–7441, 2004.
- [55] N. Dahal, I. A. Ibarra, and S. M. Humphrey, "High Surface Area Mesoporous  $\text{Co}_3\text{O}_4$  from a Direct Soft Template Route," *Journal of Materials Chemistry*, vol. 22, no. 25, pp. 12675–12681, 2012.
- [56] A. B. R. Mayer, S. H. Hausner, and J. E. Mark, "Colloidal Silver Nanoparticles

- Generated in the Presence of Protective Cationic Polyelectrolytes,” *Polymer Journal*, vol. 32, no. 1, pp. 15–22, 2000.
- [57] Z. Huang, G. Mills, and B. Hajek, “Spontaneous Formation of Silver Particles in Basic 2-Propanol,” *Journal of Physical Chemistry*, vol. 97, pp. 11542–11550, 1993.
- [58] I. Karakaya and W. T. Thompson, “The Ag-Pd (Silver-Palladium) System,” *Bulletin of Alloy Phase Diagrams*, vol. 9, no. 3, pp. 237–243, 1988.
- [59] H. Kobayashi, M. Yamauchi, R. Ikeda, and H. Kitagawa, “Atomic-level Pd–Au alloying and controllable hydrogen-absorption properties in size-controlled nanoparticles synthesized by hydrogen reduction,” *Chemical Communications*, vol. 0, pp. 4806–4808, 2009.
- [60] J. W. M. Frenken and P. Stoltze, “Are Vicinal Metal Surfaces Stable?,” *Physical Review Letters*, vol. 82, no. 17, pp. 3500–3503, 1999.
- [61] C. R. Henry, “Morphology of supported nanoparticles,” *Progress in Surface Science*, vol. 80, pp. 92–116, 2005.
- [62] E. Ringe, R. P. V. Duyne, and L. D. Marks, “Wulff Construction for Alloy Nanoparticles,” *Nano Letters*, vol. 11, pp. 3399–3403, 2011.
- [63] A. R. Tao, S. Habas, and P. Yang, “Shape Control of Colloidal Metal Nanocrystals,” *Small*, vol. 4, no. 3, pp. 310–325, 2008.
- [64] S. Tauster, “Strong Metal-Support Interaction,” *Accounts of Chemical Research*, vol. 20, no. 11, pp. 389–394, 1987.

- [65] W. Karim, C. Spreatico, A. Kleibert, J. Gobrecht, J. Vandevondele, Y. Ekinici, and J. A. Van Bokhoven, “Catalyst Support Effects on Hydrogen Spillover,” *Nature*, vol. 541, no. 7635, pp. 68–71, 2017.
- [66] S. S. Collins, M. Cittadini, C. Pecharromás, A. Martucci, and P. Mulvaney, “Hydrogen Spillover between Single Gold Nanorods and Metal Oxide Supports: A Surface Plasmon Spectroscopy Study,” *ACS Nano*, vol. 9, no. 8, pp. 7846–7856, 2015.